



# Coseismic ultramylonites: An investigation of nanoscale viscous flow and fault weakening during seismic slip

Giacomo Pozzi<sup>a,\*</sup>, Nicola De Paola<sup>a</sup>, Robert E. Holdsworth<sup>a</sup>, Leon Bowen<sup>b</sup>, Stefan B. Nielsen<sup>a</sup>, Edward D. Dempsey<sup>c</sup>

<sup>a</sup> Department of Earth Sciences, Rock Mechanics Laboratory, University of Durham, Durham, DH1 3LE, UK

<sup>b</sup> Department of Physics, University of Durham, Durham, DH1 3LE, UK

<sup>c</sup> School of Environmental Sciences, University of Hull, Hull, HU6 7RX, UK

## ARTICLE INFO

### Article history:

Received 7 November 2018

Received in revised form 25 March 2019

Accepted 28 March 2019

Available online 19 April 2019

Editor: J. Brodholt

### Keywords:

earthquakes  
weakening mechanisms  
ultramylonites  
rock mechanics  
carbonates  
EBSD

## ABSTRACT

Faults weaken during the propagation of earthquakes due to the onset of thermally-activated mechanisms, which vary depending on the rock type. Recent experimental work suggests that carbonate-hosted faults are lubricated by viscous flow in nano-granular aggregates having ultramylonitic textures. However, their frail nature has often hindered unbiased characterisation of the textures and deformation mechanisms operating at such extreme conditions (strain rates as high as  $10^4$ ), which remain so far poorly investigated and understood.

We explore the formation, evolution and deformation mechanisms of coseismic ultramylonites in carbonate-hosted faults generated during high velocity ( $1.4 \text{ m s}^{-1}$ ), displacement-controlled shear experiments in a rotary apparatus. Microstructures were analysed using integrated SEM and TEM imaging while detailed crystallographic fabrics were investigated using the electron back-scattered diffraction (EBSD) technique.

Mechanical data show that the strength of the experimental fault decays dynamically with slip, according to a characteristic four stage evolution; each stage is associated with characteristic textures. Microstructural observations show that brittle processes dominate when the fault is strong (friction coefficients  $>0.6$ ). Cataclasis, aided by twinning and crystal plasticity, operates forming an extremely comminuted shear band (mean grain size  $\sim 200 \text{ nm}$ ). As the fault starts weakening, shear localises within a well-defined principal slip zone. Here, thermally-activated grain size sensitive (GSS) and insensitive (GSI) creep mechanisms compete with brittle processes in controlling fault strength. GSI mechanisms produce strong monoclinic crystallographic preferred orientations in the slip zone, while textures and crystallographic orientations in adjacent locations do not evolve from the previous deformation stage. By the end of the transient weakening stage, the slip zone has reached a steady state thickness ( $30 \mu\text{m}$ ) and shows a nanogranular ultramylonitic texture. The intensity of the crystallographic preferred orientation in the coseismic ultramylonite is reduced compared to the previous stage, due to grain size sensitive creep mechanisms becoming gradually more dominant. As the experimental fault re-strengthens, upon deceleration to arrest, the ultramylonite may be partially reworked by brittle deformation.

Our findings show that the crystallographic orientations of transient microstructures are preserved in the slip zone of coseismic ultramylonites and in narrow, adjacent deactivated layers, where mirror-like surfaces are located. This shows that EBSD techniques can usefully be employed to determine the deformation mechanisms of coseismic ultramylonites and their evolution during earthquake slip in both experimental and, potentially, natural faults.

Crown Copyright © 2019 Published by Elsevier B.V. This is an open access article under the CC BY license (<http://creativecommons.org/licenses/by/4.0/>).

## 1. Introduction

Faults are classically viewed as the main expression of brittle deformation in the upper crust. The macroscopic to microscopic fabrics of fault zones are known to evolve with depth and tem-

perature (Sibson, 1977; Faulkner et al., 2010). However, their rheology and fault rock development are also strongly determined by a wide range of strain rates such as in slow, creeping faults to fast, seismogenic ones (e.g. Spray, 2010). An example of this dependence of fault rocks on strain rate is given by pseudotachylites (Sibson, 1977), which are found in natural faults where they form due to almost instantaneous frictional melting during the

\* Corresponding author.

E-mail address: [giacomo.pozzi@durham.ac.uk](mailto:giacomo.pozzi@durham.ac.uk) (G. Pozzi).

propagation of earthquakes. In particular, very large local strain rates can be attained during seismic slip and, as a consequence of shear heating, thermal activated processes, such as frictional melting, become a dominant factor in controlling the strength of the fault (Di Toro et al., 2006). Similarly, other thermally activated processes, such as flash heating (e.g. Goldsby and Tullis, 2011; Rice, 2006) and thermal pressurisation (e.g. Rice, 2006; Sibson, 1973) can take place and produce transient coseismic decreases in fault strength.

Recent experimental studies have also proposed that the onset of viscous deformation mechanisms in ultrafine grained fault rocks could also lead to coseismic dynamic weakening (Green et al., 2015; De Paola et al., 2015; Pozzi et al., 2018). In particular, in carbonate rocks, grain size sensitive (GSS) creep processes could become dominant, with textural and mechanical evidence pointing to the transient operation of grain boundary sliding (GBS) mechanisms (De Paola et al., 2015; Green et al., 2015). It has been shown that ultramylonite-like domains may form during seismic slip in carbonate-hosted experimental faults (Smith et al., 2015) and that they localise most of the deformation (Pozzi et al., 2018).

Ultramylonites are very fine-grained fault rocks produced by dynamic recrystallisation and creep deformation mechanisms during high-T ductile deformation (Sibson, 1977). Such deformation mechanisms are known to accommodate viscous flow and aseismic behaviour in lower crustal and lithospheric mantle shear zones deforming at low strain rates ( $\ll 10^{-8} \text{ s}^{-1}$ ). Also, these deformation mechanisms have previously been observed at high strain rates for a range of nano-phase alloys (Chandra, 2002) and ceramics (Lankford, 1996) in association with superplastic behaviour. However, their role in controlling fault strength during deformation of fine- to ultrafine-grained geological materials at high strain rates ( $> 10^2 \text{ s}^{-1}$ ) and sub-melting temperatures, characteristic of upper crustal seismic ruptures, is still poorly understood.

In this paper we document the development of coseismic ultramylonites produced experimentally at ultra-high, seismic strain rates, and describe in detail their structures by analysing their crystallographic preferred orientation (CPO) fabrics and their microstructural evolution throughout the dynamic weakening history. We use these findings to infer how deformation mechanisms compete in controlling fault strength at a nanograin scale during episodic seismic slip events.

## 2. Methods

### 2.1. Experimental procedure

Friction experiments were performed using a low to high velocity rotary shear apparatus at the Durham Rock Mechanics Laboratory using simulated fault gouge, which consists of fine grained (grainsize between 63  $\mu\text{m}$  and 90  $\mu\text{m}$ ) calcite powder. The apparatus and sample assembly are described in detail in the work of De Paola et al. (2015) (see also Hirose and Shimamoto, 2005; Pozzi et al., 2018).

Experiments were run at room temperature and dry conditions (relative humidity  $\sim 40\%$ ). Samples (1 g of gouge) were first loaded up to the maximum axial pressure  $\sigma_n = 25 \text{ MPa}$  and then sheared at velocities of  $v = 1.4 \text{ ms}^{-1}$  (calculated at the reference radius of 8.9 mm). A series of experiments were stopped after different amounts of displacement (4.5, 7, 25 and 90 cm at the reference radius) in order to document the microstructural evolution of recovered samples throughout the slip weakening history.

After each run, samples were carefully removed to preserve the full layer thickness, embedded in epoxy and cut parallel to the slip direction at a distance equal to the reference radius. This procedure preserves an X-Z cross-section, where X is parallel to the slip direction and Z is perpendicular to the shear zone boundary. The

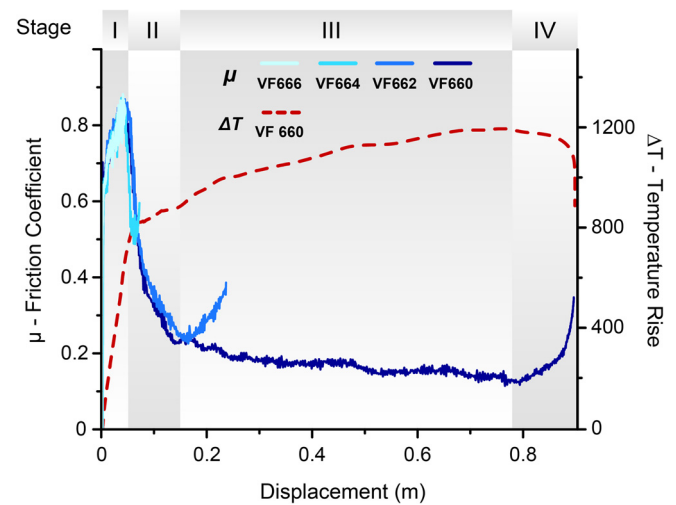


**Fig. 1.** Mechanical data ( $v = 1.4 \text{ ms}^{-1}$ ,  $\sigma_n = 25 \text{ MPa}$ ): friction coefficient ( $\mu$ , solid lines) and estimated temperature rise in the principal slip zone ( $\Delta T$ , dashed line) curves are plotted versus displacement. Temperature is calculated using a simple mono-dimensional thermal diffusion model (e.g. Rice, 2006; see also Supplementary Material 1). The four stages of friction evolution are highlighted in the graph by the shaded areas. (For interpretation of the colours in the figure(s), the reader is referred to the web version of this article.)

cut surface was then lapped with diamond paste down to 0.25  $\mu\text{m}$  and polished using colloidal silica.

### 2.2. Microstructural analysis

Microstructural analysis was carried out on polished cross-sections using a FEI Helios Dual Beam Nanolab 600 scanning electron microscope (SEM at the Department of Physics of Durham). SEM images were acquired in backscatter (BS), using the through-the-lens acquisition system, and foreshattered (FS) modes. FS is operated on 70° tilted specimens using a 4 Quadrant KE Development FS imaging control detector. Electron back-scattered diffraction (EBSD) data were collected on uncoated tilted specimens using an Oxford Instruments Nordlys HKL detector (AZtec acquisition software, Oxford Instruments). For this technique, we used a working distance of 14–15 mm and a step size of 0.2  $\mu\text{m}$ . Operating conditions were 10–20 kV of accelerating voltage and 1.4 nA current. EBSD data have been processed (including initial data cleaning) and analysed using CHANNEL5 software (HKL Technology, Oxford Instruments). Grain boundaries were defined at misorientation angles  $\geq 10^\circ$ . Grains with less than 5 data points (pixels) were discarded (i.e. with an equivalent diameter below  $\sim 0.45 \mu\text{m}$ ).

## 3. Experimental results and microstructural observations

### 3.1. Mechanical data

The experimental deformation of the calcite gouges displays a dynamic weakening history in agreement with many previous studies (e.g. Di Toro et al., 2011; Fondriest et al., 2013; De Paola et al., 2015; Siman-Tov et al., 2015; Smith et al., 2013, 2015; Pozzi et al., 2018). The friction curve follows a characteristic four stage evolution (Fig. 1). During Stage I, strain hardening behaviour is observed with friction coefficients in the Byerlee's range ( $\mu = 0.6\text{--}0.9$ ). Stage II includes the onset of dynamic weakening, following the achievement of frictional peak values, and rapid decay of the fault strength to low friction coefficients. Stage III shows low friction values ( $\mu = 0.1\text{--}0.2$ ), which continuously decrease following a very shallow slope. Stage IV takes over upon deceleration of the apparatus when the fault strength recovers up to values of

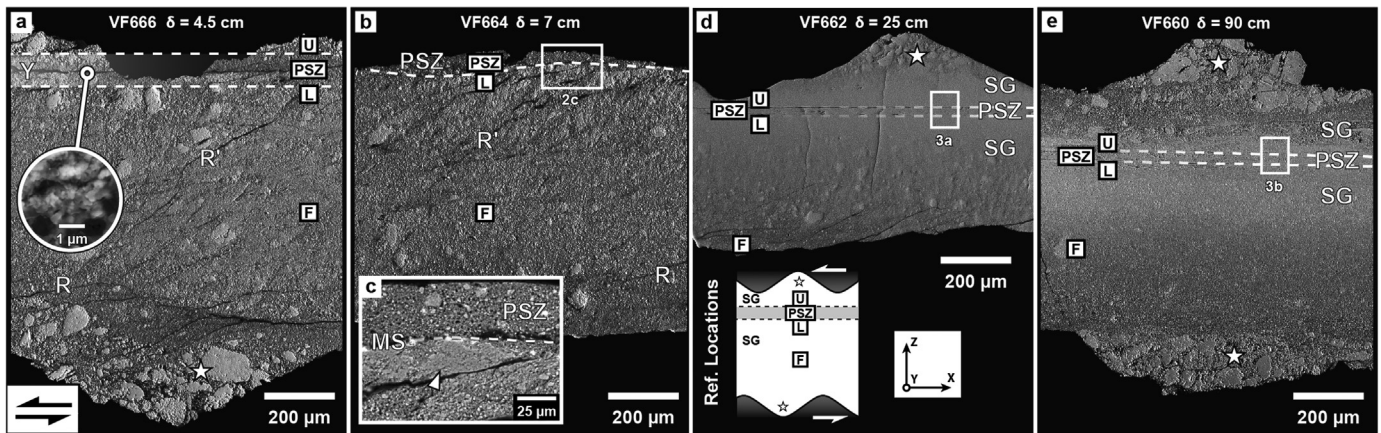


**Fig. 2.** Backscattered electron images of sample cross sections obtained from the whole thickness of gouge layers cut at the reference radius. The fault displacement,  $\delta$ , is shown for each microstructure. Relicts of the starting coarse-grained gouge are preserved in the grooves machined on the top and bottom cylinder surfaces, indicated with white stars. Shear sense is sinistral. U, PSZ, L and F squares indicate the locations where EBSD analysis has been performed (see text for details). a) Stage I: diffuse and localised deformation with Riedel shears (R, R') and a horizontal Y shear band (Y). In the inset, close-up showing the extreme grain size reduction within the Y shear band. b) Stage II: well-developed principal slip zone (PSZ) with patchy recrystallised boundary ("mirror-like surfaces", MSs). c) Close-up of area outlined in b) showing a polygonal sintered patch below an embryonic MS. d) Early Stage III: fully developed PSZ bounded by MSs and sintered, deactivated layers (sintering gradient, SG). e) Late Stage III: microstructure similar to that of early Stage III (Fig. 2d) but the SG is wider and more strongly developed. The framed U, PSZ, L and F are the reference locations (see schematic inset in Fig. 2d).

$\mu = 0.4\text{--}0.5$ . The local temperature rise (Fig. 1, red line) is calculated using a simple mono-dimensional thermal diffusion model (e.g. Rice, 2006; see Supplementary Material I).

### 3.2. Microstructure evolution throughout the weakening history

Each of the four main stages recorded throughout the weakening history is associated with a characteristic fault/shear zone architecture (Pozzi et al., 2018).

Stage I slip hardening is associated with structures and microstructures typical of the brittle regime. Samples show numerous R, R' (Riedel) shears and a shear-parallel Y shear band ( $\sim 200\ \mu\text{m}$  thick), which generally nucleates close to the top (rotating) cylinder (Fig. 2a). Brittle deformation is distributed throughout the entire gouge layer, which shows pervasive brittle grain size reduction. Extreme strain localisation occurs in the Y-shear band where grain size reduction even down to few tens of nm is observed (inset of Fig. 2a).

Following the achievement of peak friction, the Y shear band becomes a well-defined principal slip zone (PSZ) that becomes increasingly confined between sharp boundaries (Fig. 2b). In its embryonic stage, patchy volumes of polygonal grains form in the low-strain domains outside the PSZ (Fig. 2c). The recovered samples easily split along the PSZ boundaries revealing the reflective surface of the polygonal patches. These have been interpreted as the (embryonic) mirror-like surfaces (MSs) formed by sintering processes (Fondriest et al., 2013; Siman-Tov et al., 2013; Smith et al., 2013; full details in Pozzi et al., 2018). Inside the PSZ, the material is still porous and has an inhomogeneous grain size (Fig. 2c), with larger grains ( $\sim 1\ \mu\text{m}$ ) embedded in a much finer matrix ( $\sim 200\ \text{nm}$ ). At the end of Stage II - early Stage III, the PSZ has thinned by up to an order of magnitude ( $\sim 30\ \mu\text{m}$  width) and shows parallel, sharp, sintered boundaries forming continuous, flat MSs (Figs. 2d and 3a). The localisation process appears to progressively abandon several (now relict) MSs in the outer deactivated layers, a process referred to here as "MSs migration".

By Stage III, the PSZ is characterised by polygonal grains, very low porosity and homogeneous grain size ( $\sim 300\ \text{nm}$ , Fig. 3a). The crystals typically show a shape preferred orientation defining an oblique foliation, consistent with the shear sense. The texture of the PSZ itself is comparable to that of natural (Bestmann et al., 2000; Herwegh and Kunze, 2002) and experimental (Barnhoorn et

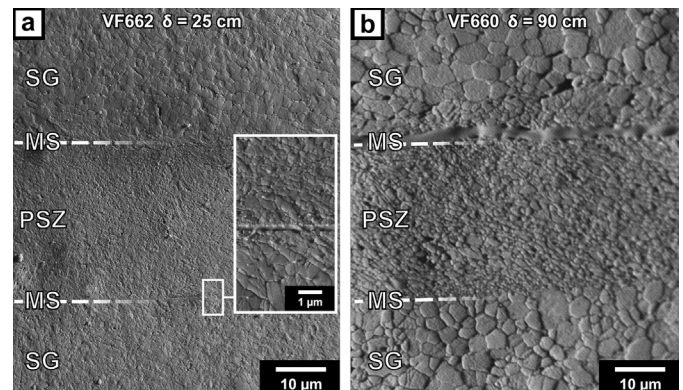


**Fig. 3.** Forescattered electron images of a) Early Stage III (close-up in the inset) and b) Late Stage III PSZ and surroundings. The PSZ maintains its thickness while grain size is observed to grow both within and outside the PSZ. Shear sense is sinistral.

al., 2004) ultramylonites. Hereafter, we refer to these textures as 'co-seismic ultramylonite' textures. The oblique foliation of the PSZ is interpreted to be the result of cycles of dynamic recrystallisation and passive rotation of grains (e.g. Barnhoorn et al., 2004, and references therein). The volumes outside the PSZ have a much coarser grain size (up to  $1\text{--}2\ \mu\text{m}$ ) and extend outward for several tens of  $\mu\text{m}$  forming a so-called 'sintering gradient' (SG; Fig. 2d; Pozzi et al., 2018). The latter is evident from the observed decrease of mean grain size and increase of porosity moving away from the PSZ.

The architecture of the PSZ and the surrounding material does not change substantially throughout Stage III. The PSZ maintains a stable thickness while the sintering gradient expands away from the PSZ and becomes stronger (Figs. 2e and 3b). Significantly, the grainsizes within the PSZ and in the sintered regions grow ( $700\ \text{nm}$  and up to  $3\text{--}4\ \mu\text{m}$ , respectively, after  $65\ \text{cm}$  of slip) with displacement and inferred rise in temperature (Fig. 3b).

Earlier formed microstructures are overprinted, but not destroyed, by the latest stages of deformation that take place upon deceleration of the machine to arrest. The Stage IV PSZ is commonly reworked and fragmented due to the effects of embrittlement. Continuous MSs are typically well preserved at the PSZ boundaries (Pozzi et al., 2018). At all stages in the experiments, the PSZ is composed exclusively of crystalline calcite showing that thermally-driven decarbonation reactions were not quantitatively significant (De Paola et al. 2015; Pozzi et al., 2018).

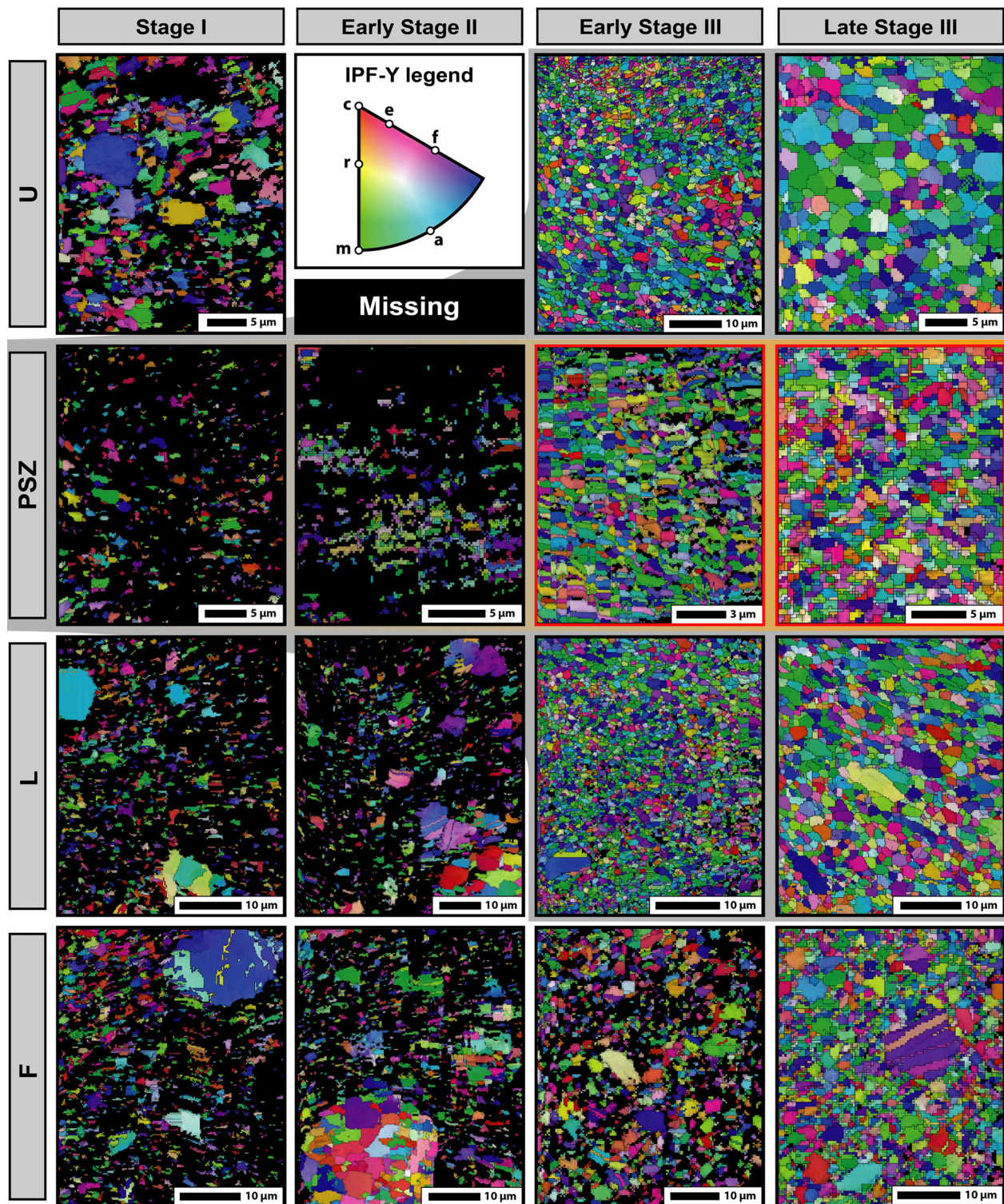


**Fig. 4.** EBSD orientation maps coloured using IPF-Y gradients. The legend shows important crystallographic directions (including c-axis and a-direction) and their IPF-Y colour. Grain boundaries (misorientation angles  $MAs \geq 10^\circ$ ) are contoured in black (better seen in Fig. SM3 in Supplementary Material III). Late Stage III U and L reference locations show that some of the larger grains are composed by coalescence of individuals sharing low  $MAs (< 10^\circ)$ , i.e. grains containing subdomains with slightly different shades of IPF colouring). (For interpretation of the colours in the figure(s), the reader is referred to the web version of this article.)

#### 4. Characteristic textures of coseismic ultramylonites revealed by EBSD data

##### 4.1. Methods

The nature and evolution of grain crystallographic orientation patterns can be investigated using electron back scattered diffrac-

tion (EBSD) analysis (e.g. Prior et al., 1999). This gives important quantitative insights into the nature and evolution of grain scale mechanisms, which can then be related to the other microstructural observations and bulk mechanical data obtained during the experimental deformation of calcite microgouges reported here.

We performed EBSD analysis on the same polished cross sections (X-Z plane) used for the microstructural characterisation. In

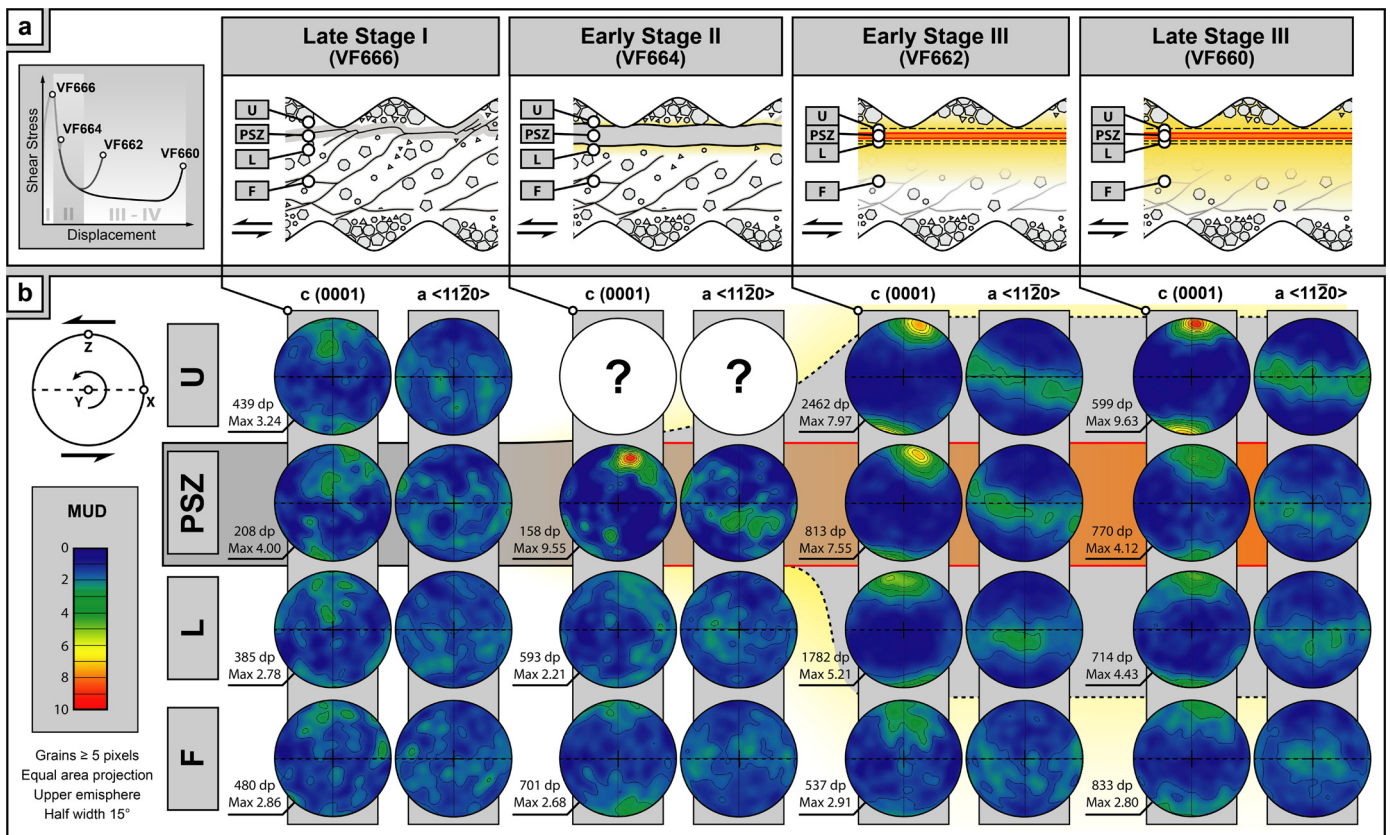


**Fig. 5.** a) Schematic representation of mechanical data, microstructures and locations of the four analysed reference areas (U, PSZ, L and F). Orange and yellow shading are used to highlight the viscous PSZ and the sintering gradient, respectively. b) EBSD pole figures (one pixel per grain, for grains  $\geq 5$  pixels) for two selected crystallographic directions for calcite: c-axis plane, (0001), and a-axis-direction,  $\langle 11\bar{2}0 \rangle$ . Poles are plotted in an equal area projection on the upper hemisphere. Multiples of uniform density (MUD) colouring applies to all of the pole figures. (For interpretation of the colours in the figure(s), the reader is referred to the web version of this article.)

particular, four critical moments of the deformation history are investigated: i) Stage I, ii) early Stage II, iii) early Stage III and iv) late Stage III (Figs. 1–2). Four distinct reference locations are selected in the samples, each preserving the characteristic deformation features of these stages (Fig. 2 and inset of Fig. 2d). One is located within the PSZ (which correspond to the Y-shear band formed during Stage I) and two lie immediately outside its boundaries, in the upper (i.e. U, towards the rotating cylinder) and lower (e.g. L, towards the stationary cylinder) outer SG layers (Figs. 2d, 5 and 6). Note that U and L positions are not fixed as the active PSZ boundaries migrate during localisation. The fourth location, F, is chosen halfway between the lower PSZ boundary and the stationary cylinder. This reference location is fixed and never lies close to the PSZ at any of the four deformation stages. Given their frail nature, samples were polished with particular care. However, as it is difficult to completely remove the grain topography, this makes the indexing of EBSD data variable, ranging from a minimum of 20% of Stage I gouges successfully measured up to 95% in the sintered layers of Stage III.

The EBSD data were processed to visualise the crystallographic orientation of calcite grains using orientation maps (Fig. 4, coloured using IPF-Y gradient), to analyse the orientation of relevant crystallographic elements with pole figures (Fig. 5, using one point per grain and plotted on equal-area projections, upper hemisphere) and to perform misorientation analyses (Fig. 6). In our samples, two representative crystallographic directions are selected: (0001) c-axis plane and  $\langle 11\bar{2}0 \rangle$  a-axis direction. Results for other directions and planes can be found in the Supplementary Material (section IV). Pole figures were contoured using the ori-

entation distribution function (Bunge, 1981) calculated with a half width of  $15^\circ$ . This value is chosen for consistency reasons with some of the cited articles (e.g. Bestmann et al., 2000; Pieri et al., 2001; Barnhoorn et al., 2004).

Due to the extremely small grain size observed locally in the samples ( $< 450$  nm), we also report in Supplementary Material V pole figures that include grains containing less than 5 pixels. These pole figures do not differ substantially from those reported (Fig. 5), but include information from small grains that might have been lost.

Misorientation analysis is used to quantify the overall distribution of crystal orientations and is utilised herein to investigate the deformation mechanisms responsible for each texture (Wheeler et al., 2001). The misorientation angle, MA, is the minimum angle describing the difference in crystallographic orientation between two grains, and can be measured for neighbouring (grains sharing a boundary) or random (randomly picked grains) pairs. Measured MAs provide an indication of the grain lattice transformation – taking into account the symmetry – that lead to differently oriented grains. The relative frequency of MAs falling within an orientation range (bins having a width of  $5^\circ$  in this work) can be plotted in a diagram for each selected range (e.g. 22 bins between  $0^\circ$  to  $110^\circ$ ), thus producing neighbour-pair and random-pair MA distributions (MAD), respectively. MAs  $< 2^\circ$  were discarded as these values lie close to the resolution of the measurements. The reference theoretical misorientation angle distribution for a random distribution (TRD) of trigonal crystals (Wheeler et al., 2001) is shown along with the MAD data in Fig. 6.

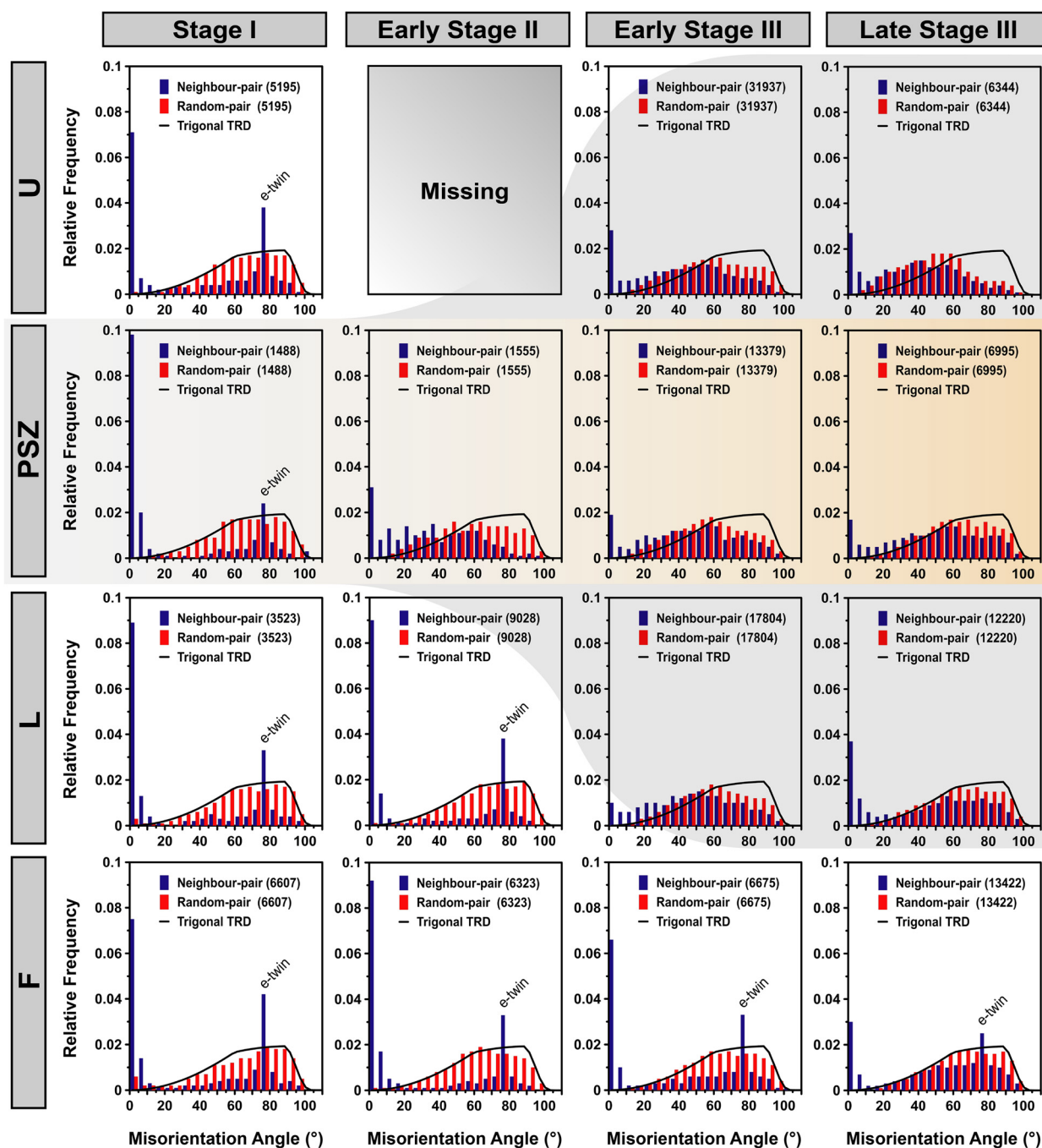


**Fig. 6.** Misorientation analysis plots showing neighbour-pair MAD (blue bars), random-pair MAD (red bars) and theoretical random distribution (TRD) for trigonal crystals (black curve). The bin width of each misorientation angle (MA) group is 5°. MAs  $< 2^\circ$  are disregarded as they lie within the resolution of measurement. (For interpretation of the colours in the figure(s), the reader is referred to the web version of this article.)

## 4.2. Results

### 4.2.1. Deformation Stage I

During Stage I, the PSZ reference location is in the proto-PSZ (the Y-shear band) while U, L and F lie in the Riedel-shear dominated sample region (Figs. 2a and 5a). The latter areas typically show a strongly heterogeneous grainsize, with larger particles ( $\gg 1 \mu\text{m}$ ) dispersed in a finer matrix; this contrasts with the more comminuted – but still heterogeneous grainsize – PSZ (mean grainsize  $\sim 200 \text{ nm}$ ). Stage I materials are poorly consolidated and porous, which hindered the polishing procedure. As a result of the topographic effects caused by the poor polish, data from loose nanoparticles could not be retrieved and large areas of

non-indexed material (dark areas) dominate the EBSD maps at this stage (Fig. 4, Stage I). Hence, the interpretation of crystallographic data is necessarily restricted to detected grains, which are overall larger than  $1 \mu\text{m}$ .

Pole figures show a relatively weak clustering of the calcite c-axes at a small angle to the Z direction, especially in the PSZ (Fig. 5b). This produces a weak crystal preferred orientation (CPO), with multiple uniform distributions (m.u.d.) smaller than 4. Each of the four reference locations produces very similar misorientation plots (Fig. 6). The neighbour-pair MAD shows a strong maximum at low MAs ( $< 10^\circ$ , MA used to separate between grain and sub-grain boundaries), with the highest frequency found in the PSZ. Another peak is located between  $75^\circ$ – $80^\circ$  MAs, the lowest of which occurs

in the PSZ (Fig. 6). This peak is likely related to e-twinning of calcite ( $e$  {01-18}; e.g. Bestmann and Prior, 2003). The random-pair MAD deviates slightly (especially in L and F locations at the low MAs,  $<10^\circ$ ) from the theoretical misorientation angle distribution for a random distribution (TRD) of trigonal crystals (TRD in Fig. 6). This is consistent with the presence of the weak CPO in all locations (Fig. 5).

#### 4.2.2. Early Deformation Stage II

During early Stage II, when the material has started to weaken, clustering of  $c$ -axes produces a strong monoclinic CPO (m.u.d. = 9.55) within the PSZ domain, tilted clockwise – consistent with the sinistral shear sense – at a small angle with respect to  $Z$ -direction (Fig. 5b). The  $a$ -axes form distinct maxima (better seen in Fig. SM8, Supplementary Material V) on the great circle lying at a low angle to the  $XY$  plane (Fig. 5b). This pattern is typical of simple shear deformation of calcite (e.g. Wenk et al., 1987). Within the PSZ, the random-pair MAD deviates from the TRD due to the development of the strong CPO. The e-twin peak disappears from the neighbour-pair MAD and the frequency of low MAs ( $<10^\circ$ ) decreases (Fig. 6). In reference locations L and F, textures and crystallographic data do not differ substantially from Stage I. The U domain could not be retrieved due to the delicate nature of the samples.

By the end of Stage II, localisation processes have ended and PSZ has reached a steady state thickness of 30  $\mu\text{m}$  (Fig. 3).

#### 4.2.3. Early Deformation Stage III

During early Stage III, the PSZ is non-porous and shows a nanogranular ultramylonitic texture. The CPO is comparable to that of the Stage II PSZ, but is slightly weaker (m.u.d. of 7.55, Fig. 5b). The dominant green and blue IPF-Y colouring indicates a prevalence of  $a$ -axis and  $m$   $<10$ - $10$  $>$  directions, respectively, parallel to the  $Y$  direction (Fig. 4). In the PSZ, the random-pair MAD is bell-shaped, centred on the MA bin between  $55$  and  $60^\circ$ , reflecting the distribution of  $a$ -maxima (Fig. 6 and Fig. SM8 in Supplementary material V). The neighbour-pair MAD is similar, but the peak at low angles has become weaker compared to previous stages.

Due to the narrowing of the PSZ (during Stage II), the U and L reference locations are now within the sintered gradient below and above the PSZ, respectively, containing the array of relict MSs (Figs. 2d and 5a). These reference locations are non-porous and their sintered texture is similar to that of the PSZ as well as their CPO, but with a different intensity (Fig. 5b). The U location shows a clear maximum at low MAs ( $<10^\circ$ , Fig. 6), while the L location has a CPO that is apparently orthorhombic, with the  $c$ -axes parallel to  $Z$  (Fig. 5b). At this stage, the F location is still porous, but shows incipient sintering (densification and recrystallisation, Figs. 3d and 4). Here the pole figure and MAD show no substantial evolution from the previous stages (Figs. 5b, 6). However, the frequency of neighbour-pair low MAs ( $<10^\circ$ ) is slightly reduced (Fig. 6).

#### 4.2.4. Late Deformation Stage III

At late Stage III, after  $\sim 75$  cm of slip, the PSZ CPO has weakened substantially (m.u.d. of 4.12, Fig. 5b) and the girdle formed by  $a$ -axes is spread over a wider area. The  $a$ -maxima have completely disappeared. The random-pair MAD distribution in the PSZ has become closer to the TRD with an increase of the frequency of  $70^\circ$ - $90^\circ$  MAs (Fig. 6). No obvious change is observed in the neighbour-pair MAD.

The CPO in the U reference location strengthens and shows a clear monoclinic symmetry (Fig. 5b). The CPO in the L reference location does not vary substantially and remains similar to previous stages and to the PSZ domain (Fig. 5b). The random-pair MAD is also comparable to that of the PSZ (Fig. 6). However, the peak at low neighbour-pair MA is now much higher. The F location is now fully sintered and it is possible to see porphyroclasts

( $>5$   $\mu\text{m}$ ) inherited from Stage I embedded in a polygonal sintered matrix (Figs. 2e and 4). Again, the pole figure has not substantially evolved (Fig. 5b) despite becoming slightly weaker. This location also maintains a similar random-pair MAD close to the TRD, while in the neighbour-pair MAD, the two peaks (e-twin and low MAs) have substantially decreased (Fig. 6).

## 5. TEM imaging

Transmission Electron Microscope imaging was carried out on a JEOL 2100F FEG TEM (Department of Physics of Durham) in order to gain further insights into nanograin-scale processes. Two thin foil samples from the U and PSZ reference locations of experiment VF660 (Late Stage III) were prepared using focused ion beam (FIB) technique. Here, TEM imaging performed in scanning mode (S-TEM) reveals polygonal aggregates of slightly elongated crystals with mean aspect ratios of 1.37 and 1.62, respectively (Fig. 7a, e).

The grains in the U location have fairly homogeneous grain sizes (mean  $D = 1.8$   $\mu\text{m}$ ) and display well-defined triple junctions and sharp crystal boundaries (Fig. 7b). These are generally straight, but locally display a slight curvature (Fig. 7b, black arrow). Grains show, on average, a homogeneous distribution of dislocation densities (Fig. 7b, c). Crystals appear fairly equant and weakly distorted (e.g. bend contours in Fig. 7a-d) and rare cavitation is observed at triple junctions (Fig. 7a, d). Dislocations are commonly elongated (hundreds of nm) and do not form large entanglements or dislocation walls (Fig. 7c, d). No subgrains are observed. Locally, some partially-healed triple junctions are found within grains (white arrow in Fig. 7d).

Grains in the PSZ are more irregular, with a mean  $D \sim 700$  nm (Fig. 7e). Grains form triple junctions, and are commonly non-equiaxed and cuspidate (Fig. 7f, white arrow), while grain boundaries are frequently curved (Fig. 7f, black arrow). Diffuse cavitation, which was not resolvable with SEM imaging, is observed at triple junctions and at grain boundary-parallel microfractures (Fig. 7e, white arrows). Grains in the PSZ contain dislocations (Fig. 7g) and neighbouring grains may have substantially different dislocation densities (e.g. Fig. 7f, compare the two grains in the centre of the picture). Curved grain boundaries are generally convex towards the most strained individual grain (Fig. 7f). Furthermore, entanglements, dislocation walls (Fig. 7h, black arrow) and subgrains (Fig. 7h, white arrow) are observed within grains with higher density of dislocations.

## 6. Discussion

### 6.1. Low vs. high (coseismic) strain rate ultramylonites

The development of calcite mylonites and ultramylonites has been intensively studied (e.g. Schmid et al., 1987; Pieri et al., 2001; Barnhoorn et al., 2004; and references therein) at a range of high temperatures, but only at relatively low strain rates ( $<10^{-3}$ ). Our new microstructural evidence and CPOs analyses show that coseismic ultramylonites can also form when initial calcite microgouges are sheared under extremely high strain rate coseismic slip conditions.

The textures of the coseismic ultramylonites described here are strikingly similar to those of ultramylonites obtained in high displacement torsion experiments carried out under elevated temperature conditions at much lower strain rates (Pieri et al., 2001; Barnhoorn et al., 2004), and predicted by theoretical studies (Wenk et al., 1987). Our mechanical data and microstructural observations show that the processes that control fault weakening of coseismic ultramylonites may not differ substantially from those observed in lower strain rate ultramylonites. However, coseismic ultramylonites must operate at the nanoscale in order to accommodate high seismic strain rates at sub-melting temperatures.

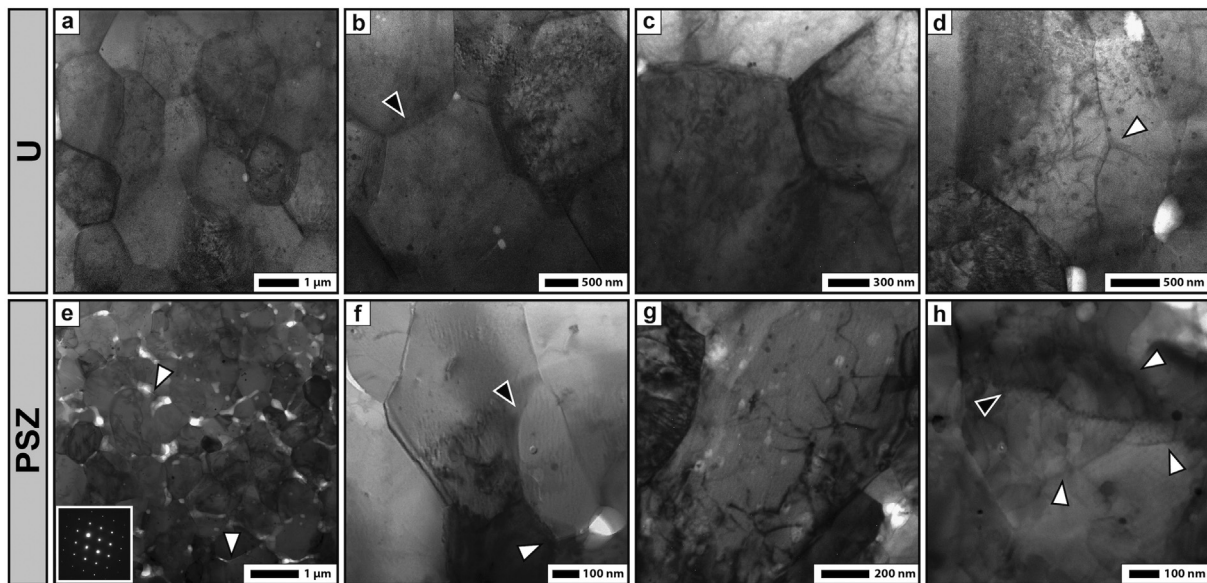


**Fig. 7.** Bright field S-TEM images of the U (a-d) and PSZ (e-h) domains of experiment VF660 ( $\delta = 90$  cm, Late Stage III). a) Equant grains displaying tightly packed structure with well-defined triple junctions and rare cavitation; b) Slight curvature of the grain boundaries (black arrow); c) Crystals containing numerous dislocations but few bend contours; d) Partially healed triple junction (white arrow) within a grain and cavitation at triple junctions (white areas). e) Sub-equant grains displaying tightly packed structure with triple junctions, diffuse cavitation (white spots) and microcracking (e.g. white arrows), inset shows a clear diffraction pattern attesting the non-amorphous nature of grains in the PSZ; f) Curved boundaries (black arrow) and cuspidate triple junctions (white arrow); g) Dislocations in a grain; h) Subgrains (e.g. white arrows) bordered by well-organised dislocation walls (e.g. black arrow).

## 6.2. Evolution of the architecture and deformation mechanisms of coseismic ultramylonites during seismic slip propagation

During high velocity friction experiments on calcite gouge, mechanical data show that the strength of the material evolves dynamically with slip, and the friction curve follows a characteristic four stage evolution (Fig. 1). Our microstructural observations reveal a shear zone-like architecture where shear localises within a PSZ from the very early stages of deformation. Hence, microstructural observations and EBSD data have been collected at four distinct reference locations: within the PSZ, in the sintered layers immediately outside the PSZ (U, L locations) and away from the PSZ (F location).

Our data show that each of the four main stages recorded throughout the weakening history is associated with characteristic microstructures in the PSZ and surrounding areas. Such observations are used below to propose a conceptual model describing the dynamic evolution of processes and deformation mechanisms associated with the development of nanometric grain size ultramylonites during seismic slip.

### 6.2.1. From gouge-cataclasite to nanometre grain size ultramylonite

During high velocity friction experiments on calcite gouge, mechanical data show that the strength of the material changes dynamically with slip, as temperature rises due to frictional heating. This suggests that, during shear localisation in the principal slipping zone, thermally activated weakening mechanisms must be dominant. Such hypotheses are supported by microstructural observations showing a transition from cataclastic shear band textures to nanoscale ultramylonites, with rising temperature during seismic slip.

- *Slip hardening behaviour during cataclastic flow (Deformation Stage I)*

During Stage I, when the deforming gouge displays slip hardening behaviour, deformation is mainly brittle preserving evidence of widespread grain size reduction and localisation into a proto-PSZ

(Y-shear band, Fig. 2a). At this stage, the material is still porous and only slightly cohesive. Random-pair MAD of the grains plots close to the trigonal TRD, suggesting that crystal orientations are only weakly influenced by the directionality of the stress field (Fig. 6). This is consistent with what is predicted to occur during cataclastic shear flow, when particles are continuously rearranged in a random fashion with increased mobility of the finer grainsizes (e.g. Hutter and Rajagopal, 1994, and references therein).

The neighbour-pair MAD reveals that two coeval plastic mechanisms take place during cataclasis. The first, e-twinning of calcite (peak at  $MA = 75^\circ - 80^\circ$ , Fig. 6), is typical of low temperature deformation regimes and is intimately related to stress concentration effects along grain contacts (Wenk et al., 1973; Schmid et al., 1987; De Bresser and Spiers, 1997). e-twinning is unable to accommodate large amounts of strain (Schmid et al., 1987; Burkhard, 1990) and we suggest that it happens at the very beginning of deformation. This process produces rotation of the calcite c-axes toward the maximum stress axis ( $\sigma'$ ) within its surrounding  $26^\circ$  small circle (Schmid et al., 1987), a mechanism possibly responsible for the weak CPO seen for Stage I in all domains in the deforming gouge layer. Alternatively, the strong peak at low MAs could be related to the activity of plastic processes such as subgrain rotation recrystallisation ( $MAs < 10^\circ$ ). This is supported by the fact that MAs below  $10^\circ$  measured in the compressed gouge (pre-shear material) are far less frequent than those observed in all reference locations during Stage I (Supplementary Material II, Fig. SM1 c).

Subgrains with dimensions ( $< 200$  nm) comparable to those of the nanograins formed during Stage I (inset of Fig. 2a) are also found in the Stage III PSZ. Such evidence supports the hypothesis that mechanisms such as shock-like stress release processes (Sammis and Ben-Zion, 2008; Spagnuolo et al., 2015) and brittle failure aided by intragranular crystal plasticity (Siman-Tov et al., 2013; De Paola et al., 2015) produce the extreme grain size reduction measured in the shear bands within the samples.

Thus, we conclude that during Stage I, the dominant strain-accommodating mechanism is brittle (Fig. 8a, c).

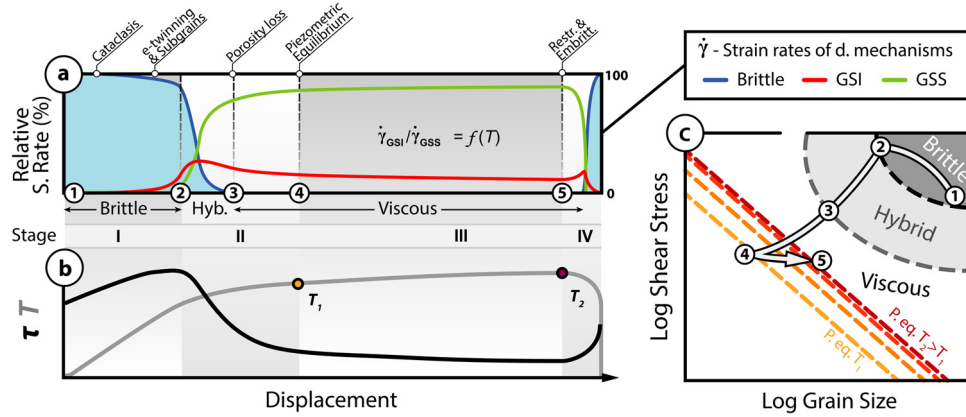


**Fig. 8.** Conceptual model for the dynamic evolution of deformation mechanisms in the PSZ constrained using microstructural evidence, including EBSD. a) Conceptual partitioning of shear strain rates ( $\dot{\gamma}$ ) accommodated by brittle (blue), grain size insensitive creep (GSI, red) and grain size sensitive creep (GSS, green) during the different Stages (I-IV) of deformation. It is assumed that at any moment, they sum to 100% of the total strain rate in the PSZ (see text for details). b) Schematic evolution of stress ( $\tau$ ) and temperature ( $T$ ) during a high velocity experiment. c) Deformation path experienced by the PSZ in a schematic deformation mechanism map. Dashed lines represent the grain size piezometric equilibrium at different moments during Stage III, where grain size is directly related to the stress state by a temperature-dependent piezometric law. Circled numbers link to the position of the event in (a). (For interpretation of the colours in the figure(s), the reader is referred to the web version of this article.)

- *Transient strength decay to quasi steady-state low strength (Deformation Stage II)*

By Stage II, the bulk temperature rise, due to frictional heating, is such that other plastic processes become competitive in accommodating strain in the PSZ. In fact, at this temperature ( $>700$  °C) and strain ( $\gg 10$ ), e-twinning is no longer efficient (De Bresser and Spiers, 1997), and so its peak completely disappears from the neighbour-pair MAD through recovery (Fig. 6). Its disappearance is also consistent with the observed pervasive grainsize reduction – below the dimension of the twins (Rowe and Rutter, 1990) – operating in the PSZ.

The deformed material becomes less porous due to yielding of nanoparticles and progressive grainsize homogenisation. The observed strong c-axis CPO in the PSZ (Fig. 5b) is explained by the operation of grain size insensitive, GSI, creep mechanisms, such as subgrain rotation ( $MAS < 10^\circ$  in Fig. 6), which operate during dynamic recrystallisation processes (dislocation creep, Fig. 8a, c).

By the end of Stage II, the PSZ is fully localised and does not substantially change its thickness throughout Stage III.

- *Viscous flow during slip at quasi steady-state low strength (Deformation Stage III)*

During Stage III, the PSZ hosts an ultramylonite with a fairly homogeneous grainsize, triple junctions and oblique foliation (Fig. 3). The strong CPO developed during Stage II is observed to progressively weaken throughout Stage III, as shown by the random-pair MAD that migrates toward the trigonal TRD (Fig. 5b). A progressive attenuation of the CPO in the PSZ could be explained by the increasing activity of diffusion creep, which is enhanced by the reduction of grainsize and temperature rise (Bestmann and Prior, 2003). Wheeler (2009) showed with his model that a transition to a diffusion-creep-dominated regime will weaken, but not destroy the CPO (see also Rutter et al., 1994). This effect is sustained by grain rotation and especially grain growth, which is observed in samples sheared throughout Stage III (Fig. 3).

However, it should be noted that the neighbour-pair MAD in the PSZ is almost identical during both the early and late Stage III (Fig. 5b). Therefore, we suggest that the major switch in rheology happens during Stage II while a quasi steady-state regime is maintained throughout Stage III (Fig. 8a, c). At the beginning of Stage III, a piezometric equilibrium – i.e. between grain size reduction operated by GSI mechanisms (e.g. see subgrains in Fig. 7h)

and grain growth driven by thermal processes – is reached within the ultramylonitic PSZ (Fig. 8a, c). At equilibrium conditions, the grain size should be directly related to the stress state, following a temperature-dependent piezometric law (e.g. De Bresser et al., 2001, 1998; Fig. 8c). Importantly, we observe that during Stage III, the mean grain size grows with slip within the PSZ (Fig. 3a and 3b, Pozzi et al., 2018), suggesting that grain size is directly related to the rising temperatures (Fig. 8c; De Bresser et al., 1998, 2001).

Our microstructural observations suggest that, during Stage III, a combination of grain size sensitive (GSS) and insensitive (GSI) creep mechanisms are active within the ultramylonitic PSZ (Fig. 8a, c). In their pioneering work, Ashby and Verrall (1973) recognised that, although GSI and GSS creep mechanisms are described by two independent flow mechanisms, they are likely to occur simultaneously in nature. In this case, the overall creep rate is given, to a sufficient approximation, by the sum of their relative contribution (Fig. 8a). The interplay between GSI and GSS creep mechanisms is well known in material sciences from observations, theory (e.g. Ashby and Verrall, 1973; Nieh et al., 1997) and modelling (Bower and Wininger, 2004; Cipoletti et al., 2011) of grain boundary sliding accommodated superplasticity. However, modelling diffusion creep coupled to intracrystalline plasticity has been an intractable problem in geoscience, leading to generic uncertainties with flow laws which combine these processes.

Therefore, we conclude that the dynamic weakening of nanometre aggregates in seismic ultramylonites involves competition between multiple and evolving temperature-dependent mechanisms, whose quantification remains so far difficult.

- *PSZ ultramylonite embrittlement and fault restrengthening during slip deceleration (Deformation Stage IV)*

During the experiments, there is always a fourth stage of deformation during sample deceleration to arrest, when the fault strength is partially recovered. The most prominent damage produced during this stage is the embrittlement of the PSZ ultramylonite, leading to splitting along the MSs (Pozzi et al., 2018). The post-mortem PSZ is a cataclasite confined between the two last active MSs. S-TEM images show embrittlement in the PSZ due to cavitation and micro-fractures (Fig. 7e), which are interpreted to form when the PSZ material moves out of piezometric equilibrium as the temperature falls. These interpretations can help explaining the restrengthening observed during Stage IV. In most cases, the

reworking of the PSZ is modest and the ultramylonitic structure is rarely completely destroyed (Fig. 3).

### 6.2.2. Shear localisation by ultramylonite boundary migration during seismic slip

Microstructures suggest that the PSZ localises during Stage II with its width reducing from 200  $\mu\text{m}$  to 30  $\mu\text{m}$  (Fig. 2a–c). This process appears to occur by the inward migration of the PSZ boundaries – MSs – in discrete, non-continuous events. Each localisation step deactivates a portion of the PSZ forming a new PSZ boundary that migrates inwards. The deactivated boundary is left in the SG domain as a relict MS. These layers, when deactivated, dramatically change their deformation regime, as they show substantial grain growth while accommodating limited amounts of deformation. This is supported by the S-TEM microstructural observations of low grain aspect ratios, straight grain boundaries and low distortion of the lattice (Fig. 7a–d).

If these hypotheses hold, the U and L locations found in the SG, and containing the abandoned MSs, should “freeze” the PSZ CPO at different moments in its evolution during Stage II. SEM images show that relict and reworked MSs are present within the U locations, but are absent within the L locations, during early Stage II (Fig. 2c). These observations show that shear localisation occurred with an asymmetric migration of the upper and lower PSZ boundaries, where the upper U location deactivated prior to the lower L location (Pozzi et al., 2018). This interpretation is strongly supported by the observation that the U location has a stronger CPO than the L location (Fig. 5b), as the latter was active longer in the PSZ, witnessing a weaker activity of the GSI creep (e.g. dislocation creep). The asymmetric migration of PSZ boundaries can be related to the fact that the U location is closer to the upper metal cylinder than the L location. Despite the cylinders having thermal properties close to those of rocks (Supplementary Materials I), they may act as more efficient heat sinks. This would promote inward (towards L) localisation of the PSZ, away from the major heat sink, where the higher temperature is found. Such asymmetric conditions are not expected to be representative of natural faults.

The grains in these deactivated regions in the SG show a grain size which is an order of magnitude larger compared to that observed in the PSZ (Figs. 2–3). Also, no outstanding variation of CPO is observed during Stage III in the L location, while the CPO in the U location has slightly strengthened (Fig. 5b). The inherited strong CPO in the U location, compared to the L location, may aid sintering processes by facilitating the coalescence of slightly misaligned neighbouring grains (e.g. partially healed triple junctions seen in some grains in Fig. 4 and Fig. 7d, black arrow). Overall, our observations suggest that grain growth in the SG locations is not influenced by dynamic recrystallisation (i.e. the same GSI and GSS creep processes operating in the PSZ no longer act in the SG region) and thus can be considered to be quasi-static. The operation of a quasi-static sintering in the SG region is also supported by the evidence of: (i) low amounts of lattice distortion in the grains (Fig. 7a–c); (ii) low dislocation entanglements (Fig. 7b–d); (iii) equant grain size (Fig. 7a); and (iv) straight grain boundaries connected by well-defined triple junctions (Fig. 7a–c). However, the increase of the low MAs ( $<10^\circ$ ) peak observed within the L location (Fig. 6) and microstructural evidence of intracrystalline plasticity within the U location (Fig. 7b–d) suggest that a relatively small degree of plastic deformation is still accommodated in the deactivated regions during Stage III and that it is coeval with sintering.

Away from the PSZ, the Riedel-populated F location is no longer sheared after Stage I, and becomes overprinted by the expanding sintering front. Its neighbour-pair MAD does not change shape throughout the four stages, but shows recovery processes driven

by static recrystallisation (Fig. 5b) as illustrated by the progressive lowering of both e-twin and low MAs peaks (Fig. 6).

### 6.3. Implications for natural faults

Our experimental work has shown that ultramylonites can develop and have a significant role in controlling fault strength during seismogenic slip under upper crustal conditions. However, in nature, the mylonitic PSZ would experience a more protracted deceleration phase than in the experiments (with lower velocity rate), as the velocity profile of seismic slip along faults follows that of a modified Yoffe function (Fukuyama and Mizoguchi, 2010 and references therein). Hence, it is expected that the more protracted re-strengthening of the fault may produce more brittle damage than observed during the experiments (Stage IV), potentially overprinting/obliterating the coseismic ultramylonite fabric within the PSZ. Liao et al. (2014) show that slow deceleration of the apparatus brings the experimental fault back to friction values in the Byerlee range ( $>0.6$ ), which are observed during the cataclastic flow of Stage I.

Arrays of parallel MSs and MSs-bounded cataclasites in seismic natural faults have been described in the published literature (Collettini et al., 2014; Tesei et al., 2013; Siman-Tov et al., 2013). Other authors who performed similar experiments have also suggested that reflective, nanograin decorated surfaces found in exhumed carbonate-hosted faults might form during earthquakes (Fondriest et al., 2013; Siman-Tov et al., 2013; Smith et al., 2013). These microstructures are indeed observed to form in our and their samples (MSs) after high velocity shear deformation. Importantly, other authors have shown that similar microstructures can form even at subseismic slip rates and thus that cannot be used in isolation as reliable seismic proxies (Verberne et al., 2013; Tesei et al., 2017).

Pozzi et al. (2018) argue that MSs are formed during the late stage embrittlement of the PSZ boundaries. It is shown that deceleration of the system produces a pervasive brittle overprint, which is enhanced at lower temperatures (i.e. as seen in lower velocity experiments).

In this scenario, it is the hardened sintered layer outside the PSZ which would stand a better chance of being preserved in natural seismic faults. Our results have shown that the sintered layers below the MSs contain important information about the ultramylonite deformation history. In particular, EBSD analysis has been shown to be a powerful tool that can be used to extract further information from microstructures that may otherwise have been overlooked in previous studies of natural fault rocks. This technique can usefully be employed in the analysis of natural MSs and it may be possible to discriminate whether they formed due to their seismic or aseismic slip, as the EBSD characteristics and patterns of the surrounding sintered regions should show a different slip history in response to different conditions in the PSZ.

## 7. Conclusions

The integration of mechanical data with microstructural observations and EBSD analyses shows that coseismic ultramylonites form in carbonate-hosted faults and follow a complex weakening path. In particular, the weakening of initial calcite microgouges when sheared at earthquake slip rates is controlled by the competition between brittle (e.g. cataclastic flow) and viscous creep deformation mechanisms. Therefore, we conclude that:

- Thermally activated grain size sensitive (GSS) and insensitive (GSI) creep mechanisms lead to the formation of coseismic ultramylonites when calcite gouges are sheared at extreme strain rate conditions. Compared to ultramylonites which form

deeper in the Earth under lower strain rate conditions, coseismic ultramylonites must form at the nanoscale in order to accommodate high seismic strain.

- The combined and simultaneous action of GSI and GSS mechanisms may lead to a grain size piezometric equilibrium in the coseismic ultramylonite PSZ, due to cycles of grain size reduction due to the operation of GSI mechanisms and grain growth driven by thermal processes.
- The crystallographic orientations of transient microstructures are preserved in the narrow deactivated layers close to the principal slip zone. Hence, EBSD techniques can usefully be employed in the analysis of microstructures associated with natural mirror-like surfaces, which are preserved in both experimental and exhumed natural faults.

## Acknowledgements

We thank M. Demurtas for his constructive reviews. We also thank Dr. Budhika Mendis for his skilled assistance with the acquisition of TEM images, Dr. A. Ceccato for his helpful advices on the EBSD methods. This project has received funding from the European Union's Horizon 2020 (Marie Skłodowska-Curie actions) research and innovation program under the Marie Skłodowska-Curie grant agreement No. 642029 - ITN CREEP, and the Natural Environment Research Council (NERC) through a NERC standard grant NE/H021744/1.

## Appendix A. Supplementary material

Supplementary material related to this article can be found online at <https://doi.org/10.1016/j.epsl.2019.03.042>.

## References

- Ashby, M.F., Verrall, R.A., 1973. Diffusion-accommodated flow and superplasticity. *Acta Metall.* 21 (2), 149–163. [https://doi.org/10.1016/0001-6160\(73\)90057-6](https://doi.org/10.1016/0001-6160(73)90057-6).
- Barnhoorn, A., Bystricky, M., Burlini, L., Kunze, K., 2004. The role of recrystallisation on the deformation behaviour of calcite rocks: large strain torsion experiments on Carrara marble. *J. Struct. Geol.* 26, 885–903. <https://doi.org/10.1016/j.jsg.2003.11.024>.
- Bestmann, M., Kunze, K., Matthews, A., 2000. Evolution of a calcite marble shear zone complex on Thassos Island, Greece: microstructural and textural fabrics and their kinematic significance. *J. Struct. Geol.* 22 (11–12), 1789–1807. [https://doi.org/10.1016/S0191-8141\(00\)00112-7](https://doi.org/10.1016/S0191-8141(00)00112-7).
- Bestmann, M., Prior, D.J., 2003. Intragranular dynamic recrystallization in naturally deformed calcite marble: diffusion accommodated grain boundary sliding as a result of subgrain rotation recrystallization. *J. Struct. Geol.* 25 (10), 1597–1613. [https://doi.org/10.1016/S0191-8141\(03\)00006-3](https://doi.org/10.1016/S0191-8141(03)00006-3).
- Bower, A.F., Wininger, E., 2004. A two-dimensional finite element method for simulating the constitutive response and microstructure of polycrystals during high temperature plastic deformation. *J. Mech. Phys. Solids* 52 (6), 1289–1317. <https://doi.org/10.1016/j.jmps.2003.11.004>.
- Bunge, H.J., 1981. Fabric analysis by orientation distribution functions. *Tectonophysics* 78 (1–4), 1–21. [https://doi.org/10.1016/0040-1951\(81\)90003-2](https://doi.org/10.1016/0040-1951(81)90003-2).
- Burkhard, M., 1990. Ductile deformation mechanisms in micritic limestones naturally deformed at low temperatures (150–350 °C). Special Publications. Geological Society of London, vol. 54(1). Geological Society, London, pp. 241–257.
- Chandra, N., 2002. Constitutive behavior of superplastic materials. *Int. J. Non-Linear Mech.* 37 (3), 461–484. [https://doi.org/10.1016/S0020-7462\(01\)00021-X](https://doi.org/10.1016/S0020-7462(01)00021-X).
- Cipoletti, D.E., Bower, A.F., Krajewski, P.E., 2011. A microstructure-based model of the deformation mechanisms and flow stress during elevated-temperature straining of a magnesium alloy. *Scr. Mater.* 64 (10), 931–934. <https://doi.org/10.1016/j.scriptamat.2010.12.033>.
- Colletti, C., Carpenter, B.M., Viti, C., Cruciani, F., Mollo, S., Tesi, T., Trippetta, F., Valoroso, L., Chiaraluce, L., 2014. Fault structure and slip localization in carbonate-bearing normal faults: an example from the Northern Apennines of Italy. *J. Struct. Geol.* 67 (Part A), 154–166. <https://doi.org/10.1016/j.jsg.2014.07.017>.
- De Bresser, J.H.P., Spiers, C.J., 1997. Strength characteristics of the r, f, and c slip systems in calcite. *Tectonophysics* 272 (1), 1–23. [https://doi.org/10.1016/S0040-1951\(96\)00273-9](https://doi.org/10.1016/S0040-1951(96)00273-9).
- De Bresser, J.H.P., Peach, C.J., Reijs, J.P.J., Spiers, C.J., 1998. On dynamic recrystallization during solid state flow: effects of stress and temperature. *Geophys. Res. Lett.* 25 (18), 3457–3460. <https://doi.org/10.1029/98GL02690>.
- De Bresser, J.H.P., Ter Heege, J.H., Spiers, C.J., 2001. Grain size reduction by dynamic recrystallization: can it result in major rheological weakening? *Int. J. Earth Sci.* 90 (1), 28–45. <https://doi.org/10.1016/S005310000149>.
- De Paola, N., Holdsworth, R.E., Viti, C., Colletti, C., Bullock, R., 2015. Can grain size sensitive flow lubricate faults during the initial stages of earthquake propagation? *Earth Planet. Sci. Lett.* 431, 48–58. <https://doi.org/10.1016/j.epsl.2015.09.002>.
- Di Toro, G., Han, R., Hirose, T., De Paola, N., Nielsen, S., Mizoguchi, K., Ferri, F., Cocco, M., Shimamoto, T., 2011. Fault lubrication during earthquakes. *Nature* 471 (7339), 494–498. <https://doi.org/10.1038/nature09838>.
- Di Toro, G., Hirose, T., Nielsen, S., Pennacchioni, G., Shimamoto, T., 2006. Natural and experimental evidence of melt lubrication of faults during earthquakes. *Science* 311 (5761), 647–649. <https://doi.org/10.1126/science.1121012>.
- Faulkner, D.R., Jackson, C.A.L., Lunn, R.J., Schlische, R.W., Shipton, Z.K., Wibberley, C.A.J., Withjack, M.O., 2010. A review of recent developments concerning the structure, mechanics and fluid flow properties of fault zones. *J. Struct. Geol.* 32 (11), 1557–1575. <https://doi.org/10.1016/j.jsg.2010.06.009>.
- Fondriest, M., Smith, S.A.F., Candela, T., Nielsen, S.B., Mair, K., Toro, Di, G., 2013. Mirror-like faults and power dissipation during earthquakes. *Geology* 41 (11), 1175–1178. <https://doi.org/10.1130/G34641.1>.
- Fukuyama, E., Mizoguchi, K., 2010. Constitutive parameters for earthquake rupture dynamics based on high-velocity friction tests with variable sliprate. *Int. J. Fract. Mech.* 163 (1–2), 15–26. <https://doi.org/10.1007/s10704-009-9417-5>.
- Goldsbey, D.L., Tullis, T.E., 2011. Flash heating leads to low frictional strength of crustal rocks at earthquake slip rates. *Science* 334 (6053), 216–218. <https://doi.org/10.1126/science.1207902>.
- Green II, H.W., Shi, F., Bozhilov, K., Xia, G., Reches, Z., 2015. Phase transformation and nanometric flow cause extreme weakening during fault slip. *Nat. Geosci.* 8 (6), 484–489. <https://doi.org/10.1038/ngeo2436>.
- Herwegh, M., Kunze, K., 2002. The influence of nano-scale second-phase particles on deformation of fine grained calcite mylonites. *J. Struct. Geol.* 24 (9), 1463–1478. [https://doi.org/10.1016/S0191-8141\(01\)00144-4](https://doi.org/10.1016/S0191-8141(01)00144-4).
- Hirose, T., Shimamoto, T., 2005. Growth of molten zone as a mechanism of slip weakening of simulated faults in gabbro during frictional melting. *J. Geophys. Res., Solid Earth* 110 (B5), B05202. <https://doi.org/10.1029/2004JB003207>.
- Hutter, K., Rajagopal, K.R., 1994. On flows of granular materials. *Contin. Mech. Thermodyn.* 6 (2), 81–139. <https://doi.org/10.1007/BF01140894>.
- Lankford, J., 1996. High strain rate compression and plastic flow of ceramics. *J. Mater. Sci. Lett.* 15 (9), 745–750. <https://doi.org/10.1007/BF00274593>.
- Liao, Z., Chang, J.C., Reches, Z., 2014. Fault strength evolution during high velocity friction experiments with slip-pulse and constant-velocity loading. *Earth Planet. Sci. Lett.* 406, 93–101. <https://doi.org/10.1016/j.epsl.2014.09.010>.
- Nieh, T.G., Wadsworth, J., Sherby, O.D., 1997. *Superplasticity in Metals and Ceramics*. Cambridge University Press.
- Pieri, M., Kunze, K., Burlini, L., Stretton, I., Olgaard, D.L., Burg, J.-P., Wenk, H.-R., 2001. Texture development of calcite by deformation and dynamic recrystallization at 1000 K during torsion experiments of marble to large strains. *Tectonophysics* 330 (1–2), 119–140. [https://doi.org/10.1016/S0040-1951\(00\)00225-0](https://doi.org/10.1016/S0040-1951(00)00225-0).
- Pozzi, G., De Paola, N., Nielsen, S.B., Holdsworth, R.E., Bowen, L., 2018. A new interpretation for the nature and significance of mirror-like surfaces in experimental carbonate-hosted seismic faults. *Geology* 46 (7), 583–586. <https://doi.org/10.1130/G40197.1>.
- Prior, D.J., Boyle, A.P., Brenker, F., Cheadle, M.C., Day, A., Lopez, G., Peruzzo, L., Potts, G.J., Reddy, S., Spiess, R., Timms, N.E., Trimby, P., Wheeler, J., Zetterström, L., 1999. The application of electron backscatter diffraction and orientation contrast imaging in the SEM to textural problems in rocks. *Am. Mineral.* 84, 1741–1759.
- Rice, J.R., 2006. Heating and weakening of faults during earthquake slip. *J. Geophys. Res., Solid Earth* 111 (B5), B05311. <https://doi.org/10.1029/2005JB004006>.
- Rowe, K.J., Rutter, E.H., 1990. Palaeostress estimation using calcite twinning: experimental calibration and application to nature. *J. Struct. Geol.* 12 (1), 1–17. [https://doi.org/10.1016/0191-8141\(90\)90044-Y](https://doi.org/10.1016/0191-8141(90)90044-Y).
- Rutter, E.H., Casey, U.K.M., Burlini, L., 1994. Preferred crystallographic orientation development during the plastic and superplastic flow of calcite rocks. *J. Struct. Geol.* 16 (10), 1431–1446.
- Sammis, C.G., Ben-Zion, Y., 2008. Mechanics of grain-size reduction in fault zones. *J. Geophys. Res., Solid Earth* 113 (B2), B02306. <https://doi.org/10.1029/2006JB004892>.
- Schmid, S.M., Panozzo, R., Bauer, S., 1987. Simple shear experiments on calcite rocks: rheology and microfabric. *J. Struct. Geol.* 9 (5), 747–778. [https://doi.org/10.1016/0191-8141\(87\)90157-X](https://doi.org/10.1016/0191-8141(87)90157-X).
- Sibson, R.H., 1973. Interactions between temperature and pore-fluid pressure during earthquake faulting and a mechanism for partial or total stress relief. *Nature* 243, 66–68. <https://doi.org/10.1038/physci243066a0>.
- Sibson, R.H., 1977. Fault rocks and fault mechanisms. *J. Geol. Soc.* 133 (3), 191–213. <https://doi.org/10.1144/gsjgs.133.3.0191>.
- Siman-Tov, S., Aharonov, E., Sagy, A., Emmanuel, S., 2013. Nanograins form carbonate fault mirrors. *Geology* 41 (6), 703–706. <https://doi.org/10.1130/G34087.1>.
- Siman-Tov, S., Aharonov, E., Boneh, Y., Reches, Z., 2015. Fault mirrors along carbonate faults: formation and destruction during shear experiments. *Earth Planet. Sci. Lett.* 430, 367–376. <https://doi.org/10.1016/j.epsl.2015.08.031>.

- Smith, S.A.F., Di Toro, G., Kim, S., Ree, J.-H., Nielsen, S., Billi, A., Spiess, R., 2013. Co-seismic recrystallization during shallow earthquake slip. *Geology* 41 (1), 63–66. <https://doi.org/10.1130/G33588.1>.
- Smith, S.A.F., Nielsen, S., Di Toro, G., 2015. Strain localization and the onset of dynamic weakening in calcite fault gouge. *Earth Planet. Sci. Lett.* 413, 25–36. <https://doi.org/10.1016/j.epsl.2014.12.043>.
- Spagnuolo, E., Plümpner, O., Violay, M., Cavallo, A., Di Toro, G., 2015. Fast-moving dislocations trigger flash weakening in carbonate-bearing faults during earthquakes. *Sci. Rep.* 5, 1–11. <https://doi.org/10.1038/srep16112>.
- Spray, J.G., 2010. Frictional melting processes in planetary materials: from hypervelocity impact to earthquakes. *Annu. Rev. Earth Planet. Sci.* 38 (1), 221–254. <https://doi.org/10.1146/annurev.earth.031208.100045>.
- Tesei, T., Collettini, C., Viti, C., Barchi, M.R., 2013. Fault architecture and deformation mechanisms in exhumed analogues of seismogenic carbonate-bearing thrusts. *J. Struct. Geol.* 55, 167–181. <https://doi.org/10.1016/j.jsg.2013.07.007>.
- Tesei, T., Carpenter, B.M., Giorgetti, C., Scuderi, M.M., Sagy, A., Scarlato, P., Collettini, C., 2017. Friction and scale-dependent deformation processes of large experimental carbonate faults. *J. Struct. Geol.* 100, 12–23. <https://doi.org/10.1016/j.jsg.2017.05.008>.
- Verberne, B.A., Spiers, C.J., Niemeijer, A.R., De Bresser, J.H.P., De Winter, D.A.M., Plümpner, O., 2013. Frictional properties and microstructure of calcite-rich fault gouges sheared at sub-seismic sliding velocities. *Pure Appl. Geophys.* 171 (10), 2617–2640. <https://doi.org/10.1007/s00024-013-0760-0>.
- Wenk, H.R., Venkatasubramanian, C.S., Baker, D.W., Turner, F.J., 1973. Preferred orientation in experimentally deformed limestone. *Contrib. Mineral. Petrol.* 38 (2), 81–114. <https://doi.org/10.1007/BF00373875>.
- Wenk, H.R., Takeshita, T., Bechler, E., Erskine, B.G., Matthies, S., 1987. Pure shear and simple shear calcite textures. Comparison of experimental, theoretical and natural data. *J. Struct. Geol.* 9 (5–6), 731–745. [https://doi.org/10.1016/0191-8141\(87\)90156-8](https://doi.org/10.1016/0191-8141(87)90156-8).
- Wheeler, J., 2009. The preservation of seismic anisotropy in the Earth's mantle during diffusion creep. *Geophys. J. Int.*, 1723–1732. <https://doi.org/10.1111/j.1365-246X.2009.04241.x>.
- Wheeler, J., Prior, D., Jiang, Z., Spiess, R., Trimby, P., 2001. The petrological significance of misorientations between grains. *Contrib. Mineral. Petrol.* 141 (1), 109–124. <https://doi.org/10.1007/s004100000225>.